

1 **Optimization of 3D controlled ELM-free state with recovered global confinement**
2 **for tokamak fusion plasmas**

3 S.K.Kim,¹ R.Shousha,¹ S.H.Hahn,² A.O.Nelson,¹ J.Wai,¹ S.M.Yang,³ J.-K.Park,³
4 R.Nazikian,³ Y.M.Jeon,² Y.In,⁴ J.H.Lee,² J.Kim,² C.Y. Lee,⁵ Y.-S. Na,⁵ and
5 E.Kolemen^{1,3}

6 ¹*Princeton University*

7 ²*Korea Institute of Fusion Energy*

8 ³*Princeton Plasma Physics Laboratory*

9 ⁴*Ulsan National Institute of Science Technology*

10 ⁵*Seoul National University*

11 (Dated: 14 July 2021)

12 Mitigation of deleterious heat flux from edge-localized modes (ELMs) on fusion reactors
13 is often attempted with 3D perturbations of the confining magnetic fields. However, the
14 established technique of resonant magnetic perturbations (RMPs) also degrades plasma
15 performance, complicating implementation on future fusion reactors. In this paper, we
16 introduce an adaptive real-time control scheme as a viable approach to simultaneously
17 achieve both ELM-free states and recovered high-confinement ($\beta_N \sim 1.91$, $\beta_p \sim 1.53$, and
18 $H_{98} \sim 0.9$), demonstrating successful handling of a volatile complex system through adap-
19 tive measures. We show that, by exploiting a salient hysteresis process to adaptively min-
20 imize the RMP strength, stable ELM suppression can be achieved while actively encour-
21 aging confinement recovery. This is made possible by a self-organized transport response
22 in the plasma edge which reinforces the confinement improvement through a widening of
23 the ion pedestal and promotes control stability, in contrast to the deteriorating effect on
24 performance observed in standard RMP experiments. These results establish the real-time
25 approach as an up-and-coming solution towards an optimized ELM-free state, which is
26 an important step for the operation of ITER and reactor-grade tokamak plasmas. Notably,
27 the real-time adaptive control scheme introduced here provides a path towards economic
28 fusion reactors by maximizing the fusion gain while minimizing damage to machine com-
29 ponents.

30 For any fusion energy source to be viable in the global marketplace, it must be able to produce
31 large amounts of electricity without incurring significant damage on the machine. The leading ap-
32 proach towards this goal is a tokamak run robustly in the high confinement mode (H-mode), which
33 is characterized by a narrow edge transport barrier responsible for significantly elevated plasma
34 pressures throughout the device¹. This “pedestal” not only enhances performance in the core re-
35 gion but also increases the non-inductive current, improving the fusion economy by reducing the
36 external heating and recirculating power required for steady-state operation. Because of these ad-
37 vantages, the ITER baseline scenario² plans to utilize H-mode plasmas to demonstrate ignition in
38 a tokamak for the first time. However, H-mode also presents serious risks to reactor operation,
39 most prominently through the creation of dangerous edge instabilities called edge localized modes
40 (ELMs)³. These rapid relaxations of the pedestal density and temperature result in intense tran-
41 sient heat fluxes on the reactor walls, leading to undesired material erosion and surface melting
42 which will not be acceptable in a reactor scenario^{4,5}. Therefore, to retain the tokamak design as a
43 viable option for fusion reactors, it is critical that we develop methods to routinely suppress ELM
44 events without degrading the plasma performance.

45 One of the most effective methods to control ELMs is to apply resonant magnetic perturba-
46 tions (RMPs) using 3D coils⁶⁻⁹. RMPs suppress ELMs by causing additional transport¹⁰⁻²³ in
47 the pedestal, degrading its height to a point where ELMs are no longer unstable²⁴⁻²⁶. However,
48 this inevitably comes at the considerable expense of global confinement deterioration, decreased
49 access to high-performance plasma regimes and thus depleted economic prospects. This degrada-
50 tion tends to be greater with a lower toroidal wave number (n) of RMP. Even so, the use of low- n
51 configurations will be important at the reactor level due to the strong decay of external fields in the
52 thick shielding between the plasma and field coils. Undoubtedly, the compatibility of RMP ELM
53 suppression with high confinement operation requires urgent exploration.

54 In this context, we report on an adaptive RMP scheme capable of maximizing plasma perfor-
55 mance while maintaining robust ELM suppression. With this new technique, up to $\sim 70\%$ of the
56 RMP-induced performance degradation can be quickly recovered, returning the plasma to a high-
57 power state suitable for future reactors. By exploiting a salient hysteresis process on the KSTAR
58 tokamak²⁷, we find that RMP-induced transport does not just produce a negative influence on
59 confinement (as is typically assumed) but instead also opens up a pathway to strong recovery of
60 plasma performance that is accessible to a highly-optimized controller. This leads to the concu-
61 rent establishment of high confinement plasmas and sustained ELM suppression at normalized

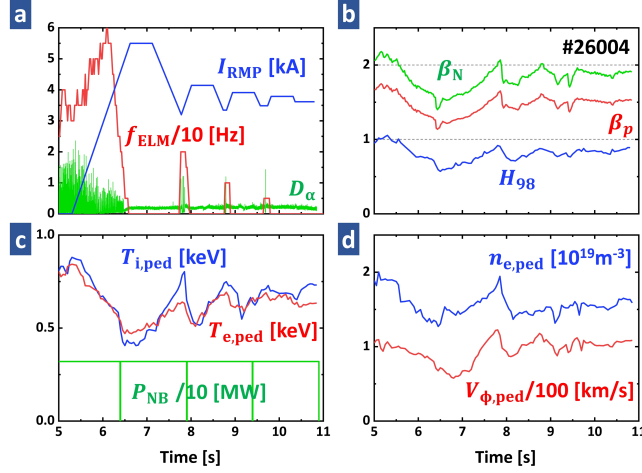


FIG. 1. **Plasma parameters for an ELM suppression discharge (#26004) with adaptive RMP control.** **a** RMP coil current (blue), D_α emission (green) near outer divertor target, and detected ELM frequency (red). **b** H_{98} (blue), β_N (green), and β_p (red). **c** Pedestal height of ion (red), electron (blue) temperature, and NBI heating power (green). **d** Pedestal height of electron density (blue) and toroidal rotation of carbon (6+) impurity (red).

62 performance close to the ITER-baseline level, reaching $\beta_N \sim 1.91$, $\beta_p \sim 1.53$, and $H_{98} \sim 0.9$.
63 Here, $\beta_N = \frac{aB_T}{I_p} \frac{p}{B^2/2\mu_0}$ is the normalized beta, $\beta_p = \frac{p}{B_p^2/2\mu_0}$ is the poloidal beta, and $H_{98} = \tau_{\text{exp}}/\tau_{98}$
64 is the thermal energy confinement quality compared to the standard H-mode plasmas, where p is
65 the averaged plasma pressure, a is the minor radius, I_p is the total plasma, B_T is the toroidal mag-
66 netic field, B_p is the poloidal magnetic field, B is the total magnetic field, τ_{exp} is the experimental
67 thermal energy confinement time, and τ_{98} is the empirically derived confinement time using stan-
68 dard H-mode database²⁸. Since H_{98} enters to the power of 3.23 in determining the fusion gain
69 Q_{fus} ²⁹, where Q_{fus} is the ratio between produced fusion energy over input, the strong recovery of
70 H_{98} demonstrated in this work allows a substantial reduction of fusion cost, establishing a means
71 with which RMPs can be used for ELM suppression to enable commercial-grade fusion devices.

72 I. RESULTS

73 **Optimized pedestal using adaptive control.** Figure.1 shows an example of H-mode plasma
74 with fully suppressed ELMs via adaptive feedback RMP amplitude control. In this discharge, a
75 hysteresis effect is utilized where ELM suppression can be maintained over long periods with a
76 lower RMP strength than initially required for access to the ELM suppression regime¹⁷. Because

77 reduction of the RMP amplitude leads to an increased pressure pedestal height, this enables global
78 confinement recovery in an ELM-free state³⁰ by adjusting RMP levels. To avoid ELMs while
79 maximizing the confinement, we use a preset low $n = 1$ RMP waveform⁸ and apply real-time
80 feedback to control its amplitude. During the plasma current flattop before applying RMP, with
81 $I_p = 0.51$ MA and ~ 3 MW of neutral beam injection heating, $\beta_N \sim 2.13$, $\beta_p \sim 1.71$, and $H_{98} \sim$
82 1.03 , close to the targets of the proposed ITER baseline scenario. In this discharge, the plasma
83 edge safety factor $q_{95} \sim 5$, which is higher than the target value of $q_{95} \sim 3$. Here, q_{95} is defined
84 as the pitch of the magnetic field line in the edge where the normalized poloidal flux (ψ_N) is
85 95%. However, after achieving the first stable ELM suppression through traditional means (7.1
86 s), the plasma performance significantly decreases to $\beta_N \sim 1.62$, $\beta_p \sim 1.30$, and $H_{98} \sim 0.68$. The
87 30% reduction in overall confinement by RMP mainly comes from degradation in density and
88 temperature pedestal, as shown in Fig.1c, d. Such extensive confinement and H_{98} degradation is
89 a well-known general trend in low-n RMP experiments³¹⁻³³ and will not be acceptable in a future
90 fusion reactor because this leads to a significant increase in fusion cost.

91 After this initial degradation, the real-time adaptive ELM control scheme starts to recover the
92 original performance before RMPs were introduced while maintaining stable ELM suppression.
93 The controller leverages the D_α emission signal near the outer divertor target to calculate the
94 frequency of ELMs (f_{ELM})³⁴. To achieve ELM suppression, the RMP amplitude (or coil cur-
95 rent, I_{RMP}) is raised until f_{ELM} decreases to 0, i.e., ELM suppression. Then, during the resulting
96 ELM-free period, the controller lowers the RMP strength to raise the pedestal height until ELMs
97 reappear, at which point the control again starts to ramp up the RMP amplitude until suppression
98 is recovered (Fig.1a). In the experiment presented in Fig.1, there are 0.5 s of RMP flattop intervals
99 between the RMP-ramp up and down phase to achieve saturated RMP response. Throughout this
100 process, we adjust the lower bound of I_{RMP} to match the value where the most recent ELM returns.
101 This adaptive constraint reduces the likelihood of ELM suppression loss and control oscillation.
102 The feedback system leads the plasma to a converged operating point that optimizes both ELM-
103 free operation and confinement, recovering most of the performance lost in the initial application
104 of RMP.

105 In the selected discharge, this adaptive ELM control scheme achieves a stable ELM-free phase
106 at 10.5 s with improved global confinement, as shown in Fig.1b. Although a few ELMs occur
107 before convergence, the controller successfully reaches a stable operating point with minimized
108 ELM periods. In the final state, the plasma performance shows $\beta_N \sim 1.91$, $\beta_p \sim 1.53$, and

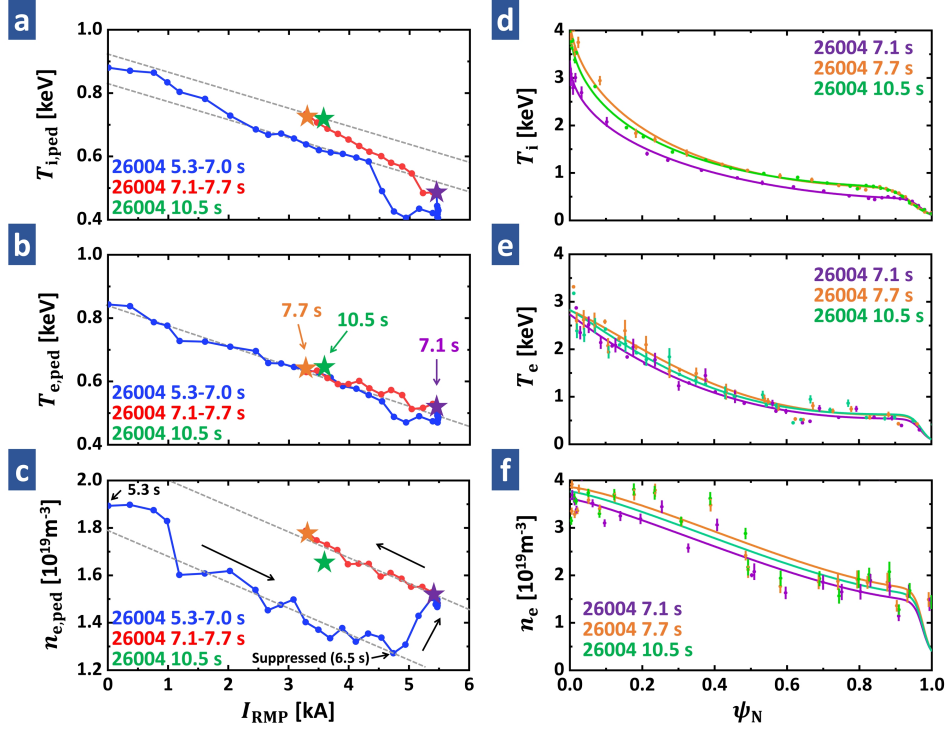


FIG. 2. Pedestal height (left) and core plasma profiles (right) for RMP ramp-up (5.3-7.1 s, blue), down (7.1-7.7 s, red), first saturated ELM-suppression (7.1 s, purple), first optimized suppression (7.7 s, orange), and finally optimized suppression (10.5 s, green). **a-c** Pedestal height of ion, electron temperature and electron density. **d-f** Core ion, electron temperature, and electron density with statistical error bars. Ion temperature is measured by a charge-exchange recombination system for carbon (6+) impurities. Electron temperature is measured by the Thomson Scattering and Electron cyclotron emission system. Electron density is measured by the Thomson Scattering and Two-color interferometry system.

109 $H_{98} \sim 0.9$, recovering up to 68% of the original confinement degradation. Such increase in H_{98}
 110 is especially important as this leads to the 60% recovery in Q_{fus} degradation, thus emphasizing
 111 the performance of adaptive control. The enhanced confinement quality occurs with the recov-
 112 ery of both the temperature and density pedestals. As can be seen in Fig.1c, d, all pedestals are
 113 significantly improved from the first ELM suppression phase. For example, electron ($T_{e,\text{ped}}$) and
 114 ion ($T_{i,\text{ped}}$) temperature pedestals increase by 22% and 50%, respectively. In addition, the electron
 115 density pedestal ($n_{e,\text{ped}}$) is also recovered by 10% at the same time. Interestingly, $H_{98} \sim 0.9$ at
 116 10.5 s is much larger than $H_{98} \sim 0.75$ at 6.2 s, even with the same $I_{\text{RMP}} = 3.6$ kA. This indicates
 117 that the confinement recovery by adaptive approach is not solely attributable to decreased I_{RMP} ,
 118 but rather that another contributor leads the plasma to a reinforced high-confinement state.

119 We note that the ion temperature pedestal exhibits significant recovery compared to the other
 120 channels. This is mainly due to the rapid and significant increase of ion pedestal height by
 121 decreasing RMP strength. The traces of pedestal height versus I_{RMP} before the first ELM reap-
 122 pearance (5.3-7.7s) reveal this trend, as shown in Fig.2a-c. $n_{\text{e,ped}}$ and $T_{\text{e,ped}}$ have a similar depen-
 123 dence on I_{RMP} during the pedestal degradation (5.3-6.5s) and recovery (7.1-7.7s) phases, showing
 124 $\frac{\Delta n_{\text{e,ped}}}{\Delta I_{\text{RMP}}} \sim -10^{15}/\text{m}^3\text{A}$ and $\frac{\Delta T_{\text{e,ped}}}{\Delta I_{\text{RMP}}} \sim -0.06 \text{ eV/A}$. However, $T_{\text{i,ped}}$ in the recovery phase shows a
 125 50% larger response of -0.09eV/A compared to the degradation phase, -0.06eV/A . The differ-
 126 ence of responses in these phases leads to the faster and larger recovery of the ion pedestal. As
 127 shown in Fig.2d-f, all radial profiles in the core plasma are almost identical during the recovery
 128 phase. Therefore, the improved confinement by decreasing RMP strength results from increased
 129 $n_{\text{e,ped}}$, $T_{\text{e,ped}}$, and $T_{\text{i,ped}}$, with the last one dominant. In particular, $\sim 67\%$ of improvement comes
 130 from the ion pedestal, and this is responsible for reinforced recovery by adaptive control. The
 131 large growth of $T_{\text{i,ped}}$ is mainly due to the simultaneously increased upper limit of $T_{\text{i,ped}}$ before the
 132 loss of ELM suppression and its enhanced response to the RMP strength. In addition, $n_{\text{e,ped}}$ shows
 133 a large increase near $I_{\text{RMP}} \sim 5 \text{ kA}$ (Fig.2c), which can be attributed to reduced particle pumping
 134 from ELMs. This occurs before 7 s and does not directly contribute to confinement recovery
 135 beginning at 7.1 s. However, it still strengthens the confinement recovery with increasing $T_{\text{i,ped}}$.
 136

137 **Advantages of the adaptive ELM control for achieving safe ELM suppression.** In standard
 138 H-mode discharges, strong RMPs are favorable for entering the ELM suppression but also raises
 139 the possibility of dangerous plasma destabilization. Too large of an RMP field in the core plasma
 140 normally leads to a locking of plasma rotation and invokes a disastrous core instability called a dis-
 141 ruption, as seen in Fig.3a. Core locking (or disruptions) terminate the plasma and forms transient
 142 heat fluxes on the tokamak walls which are even more severe than ELMs. Unfortunately, plasma
 143 disruption is easier with low-n RMPs. Therefore it is vital to maintain the RMP strength between
 144 the thresholds of ELM suppression and disruption. To complicate this process, these thresholds
 145 change in time with various plasma parameters and are often hard to theoretically predict. The
 146 database³³ for $n = 1$ RMP ELM suppression in KSTAR reveals broadly scattered experimental
 147 thresholds showing $1 \sim 2 \text{ kA}$ variations, and empirical prediction is also challenging due to their
 148 sensitivity to plasma parameters. For these reasons, in the present experiments, a series of dis-
 149 charges are used to find safe RMP strength for ELM suppression. This approach will not be
 150 applicable in a fusion reactor, where a single disruption can result in the termination of machine

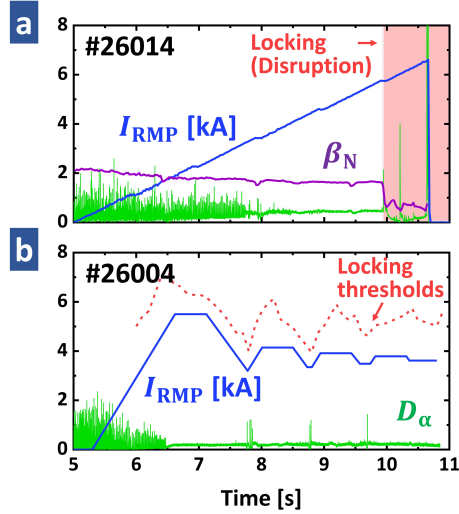


FIG. 3. Plasma parameters for a RMP-induced disruption and suppression discharge with $n = 1$ RMP in KSTAR. **a** RMP coil current (blue), D_α emission (green), and β_N (purple) of discharge #26014. Onset of locking (disruption) is marked as a red region. **b** RMP coil current (blue) and D_α emission (green) of discharge #26004. The disruption thresholds in I_{RMP} is marked as a red dotted line.

151 life.

152 Notably, the adaptive approach lowers the RMP strength after entering the ELM-free state and
 153 maintains it near the levels for marginally stable ELM suppression. This automatically avoids
 154 touching the disruptive limits. As shown in Fig.3b, the RMP strength stays safely below the dis-
 155 ruption threshold throughout the example discharge, highlighting the advantages of this adaptive
 156 scheme for achieving stable ELM suppression. Here, the disruption thresholds are predicted from
 157 adjacent RMP-disruption experiments and ideal RMP response calculations. Although adaptive
 158 RMP control will be ineffective if only a small margin exists between the thresholds for suppres-
 159 sion and disruption, it still reduces the necessity of extensive optimization of the RMP geometry
 160 for locking avoidance, which often comes at the expense of other important parameters or opera-
 161 tional degrees of freedom.

162

163 **Improved ELM stability and ion pedestal response by RMP-induced transports.** Instead of
 164 causing only degradation of pedestal, RMP-induced pedestal transport facilitates the improvement
 165 of the $T_{i,ped}$ limit and its response to the RMP strength by broadening the ion-pedestal. RMP-
 166 induced transport on the ion pedestal can be found from the analysis of the ion pedestal profiles in
 167 detail. Fig.4a, b illustrate ion pedestal and $E \times B$ flow profiles for five times between 5.3 and 7.7

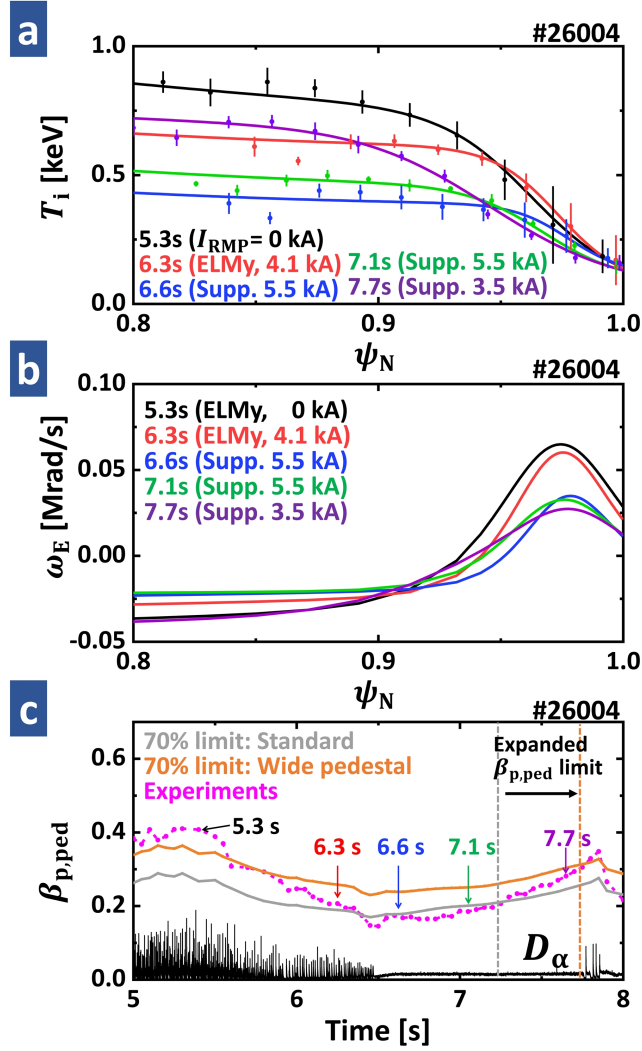


FIG. 4. **Time traces of pedestal profiles and stability limits during adaptive ELM control (#26004).** **a** Ion pedestal profiles with statistical error bars are shown for five different time slices. **b** ExB flow profiles (ω_E) at pedestal are shown for five different time slices. **c** 70% of ELM stability limit for $\beta_{p,ped}$ with (orange) and without (gray) wide ion pedestal, calculated from EPED code. Experimentally measured $\beta_{p,ped}$ (magenta) and D_α emission (black) are also shown. The dotted lines show $\beta_{p,ped}$ limits during ELM-free state imposed by pedestal stability with (gray) and without (orange) wide ion pedestal.

168 s. Before ELM suppression (5.3-6.3 s), $T_{i,ped}$ decreases with I_{RMP} , while the pedestal gradient is
 169 well sustained (or even slightly increased). After ELM suppression (> 6.5 s), however, the pedestal
 170 stiffness starts to change. The transition from 6.6 to 7.1 s shows broadening of the ion pedestal and
 171 decreasing of its gradient. This widening is maintained in the pedestal recovery phase up to 7.7
 172 s. The decrease in pedestal height and gradient are both due to RMP-induced transport. However,

173 the rapid broadening of the ion pedestal after ELM suppression indicates that its gradient is not
 174 governed by the transport affecting the pedestal height but instead by an “additional” transport
 175 source that occurs in the ELM suppression phase.

176 The change in ion pedestal width improves the ELM stability. In theory, pedestal pressure
 177 (P_{ped}) or pedestal poloidal beta ($\beta_{\text{p,ped}} = \frac{P_{\text{ped}}}{B_p^2/2\mu_0}$) should stay under the stability limit to avoid
 178 the reappearance of ELM crashes. Stability analysis confirms that $\beta_{\text{p,ped}}$ stays below 70% of the
 179 stability limit during the ELM suppression phase. This stability limit is known to improve with
 180 increased pedestal width³⁵. Therefore, widened pressure pedestal via ion-pedestal broadening
 181 allows for higher $\beta_{\text{p,ped}}$ during the ELM-free phase. Numerical analysis reveals that the $\beta_{\text{p,ped}}$
 182 limit increases by 53% due to ion pedestal broadening. This change is presented in Fig.4c. With
 183 the expansion of the $\beta_{\text{p,ped}}$ limit illustrated as dotted lines, $\beta_{\text{p,ped}}$ can further increase from 0.2
 184 (gray dotted line) to 0.31 (orange dotted line). This enhanced $\beta_{\text{p,ped}}$ limit allows access to higher
 185 $T_{\text{i,ped}}$ in the ELM suppression phase.

186 The broader ion-pedestal also can lead a larger response of $T_{\text{i,ped}}$ on RMP strength. Inspired
 187 from (Hu et al. 2020)³⁶, the change of pedestal height (ΔT_{ped}) by ΔI_{RMP} can be described as Eq.1,

$$\frac{\Delta T_{\text{ped}}}{\Delta I_{\text{RMP}}} \approx \nabla T_{\text{ped}} \sum_{m \geq q_{\text{ped}}} \frac{\partial W_{m,n}}{\partial I_{\text{RMP}}}, \quad (1)$$

188 where $W_{m,n}$ and ∇T_{ped} are the (m, n) island width and pedestal gradient, respectively. q_{ped} is an
 189 edge safety factor on the pedestal top. This expression is based on the concept where ΔT_{ped} is
 190 the accumulation of profile flattening by the islands in the pedestal region. We note that constant
 191 ∇T_{ped} over the pedestal region is assumed to make interpretation easier. This expression addresses
 192 that pedestal height changes more rapidly with RMP strength as the pedestal gradient grows and
 193 q_{ped} decreases. With the given q profile monotonic, q_{ped} is reduced by increasing pedestal width.
 194 The largely broadened ion pedestal can lead to a stronger response of $T_{\text{i,ped}}$ despite the decrease of
 195 ion pedestal gradient. In addition, ion pedestal is known to be heavily influenced by neoclassical
 196 transport^{15,37,38}. Here, neoclassical heat flux by RMPs is roughly proportional to I_{RMP}^2 , and it
 197 increases more rapidly with the smaller radial electric field and its gradient^{39,40}. Because a wide
 198 ion pedestal reduces the electric field^{19,41} at the pedestal (Fig.4b), this correlation also contributes
 199 to improving the response of $T_{\text{i,ped}}$.

200 On the other hand, the responses of $n_{\text{e,ped}}$ and $T_{\text{e,ped}}$ to RMP strength are almost identical
 201 whether or not the ELMs are fully suppressed. This means that additional RMP-induced transport
 202 in the ELM-free phase has a smaller effect on the electron density and temperature pedestal gra-

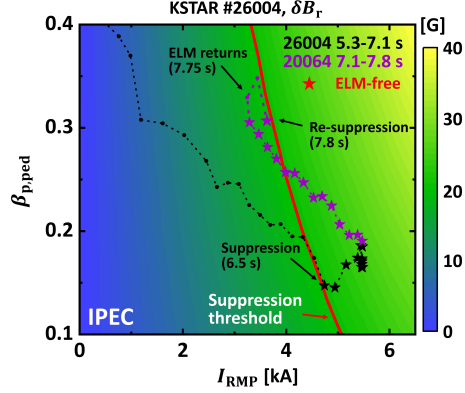


FIG. 5. **The pressure pedestal height versus RMP strength during adaptive ELM control (#26004).** The time traces of $\beta_{p,ped}$ in #26004 discharge for 5.3-7.1 s (black) and 7.1-7.8 s (purple) with varying I_{RMP} . ELM-free states are marked as star dots. Contours of δB_r at pedestal region from ideal response calculation using IPEC are also shown. Experimentally derived δB_r threshold for ELM suppression is drawn as a red curve.

203 dent. Although the electron pedestal width has considerable uncertainty due to limitations in the
 204 resolution of edge diagnostics, its value lies between 4-6% in normalized poloidal flux without
 205 showing a considerable widening like ion pedestal, suggesting that additional transport has only a
 206 relatively small effect on electron channels.

207

208 **Advantages of RMP-induced transport and wide ion pedestal in adaptive ELM control.** In-
 209 creased $T_{i,ped}$ response by RMP-induced transport leads to an extensive recovery of $T_{i,ped}$ during
 210 RMP ramp-down and makes an ion pedestal higher than the RMP ramp-up phase (ELMy) even
 211 with the same RMP strength. In addition, enhanced pedestal stability allows for larger $T_{i,ped}$ before
 212 the return of ELMs. The synergy between these effects boosts the pedestal recovery and enables
 213 adaptive control to maximize the confinement, resulting in a much higher pedestal than during the
 214 initial phase of ELM suppression, as shown in Fig.5, which illustrates $\beta_{p,ped}$ versus I_{RMP} . The
 215 changes to the pedestal from 5.3 to 7.8 s are shown, and the ELM suppressed states are marked
 216 with star points.

217 Another advantage of RMP-induced transport is that it improves the control stability. Adaptive
 218 control can be unstable due to a bifurcation of the plasma state during transitions between ELMy
 219 and ELM-free regimes, which causes oscillation of the control system. In particular, it can take
 220 a long time or even become impossible for a controller to find the optimal solution because of

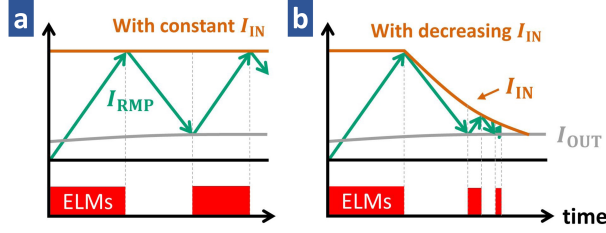


FIG. 6. **Schematic diagram of adaptive ELM control using RMPs.** Here, RMP threshold for ELM suppression entry (I_{IN} , orange) and exit (I_{OUT} , gray) are drawn. Time trace of I_{RMP} (green) and onset of ELMs (red box) are also shown. Expected time trace of adaptive ELM control with **a** constant I_{IN} and **b** decreasing I_{IN} in time.

221 the sudden jump in RMP strength required for re-entry (I_{IN}) to or exit (I_{OUT}) from ELM suppression
 222 sion. The schematic diagram in Fig.6a illustrates how this characteristic will delay the control
 223 convergence. In practice, ELM control must be done quickly to minimize damage to the reactor,
 224 so an adaptive approach is generally hard to use in such a bifurcating system. However, RMP-
 225 induced transport eases these control difficulties by reducing I_{IN} during adaptive control, as shown
 226 in Fig.6b.

227 It has been shown that the plasma enters the ELM suppression state above a certain δB_r
 228 threshold⁴², where δB_r is the perturbed radial field strength at the pedestal. This threshold (~ 20
 229 G) for the reference discharge is shown as the red contour of Fig.5. Here, $\beta_{p,ped}$ amplifies the per-
 230 turbed field⁴², and the same δB_r can be obtained with a smaller I_{RMP} with larger $\beta_{p,ped}$. Because
 231 RMP-induced transport enhances $\beta_{p,ped}$ in an ELM-free state, this leads to a lower I_{IN} , making
 232 access to the next ELM suppression regime easier. The ELM suppression of 7.8 s shown in Fig.5
 233 results from reduced I_{IN} compared to the former one at 6.5 s. Thus, I_{IN} for each suppression
 234 entry changes as $4.9 \rightarrow 3.6 \rightarrow 3.53 \rightarrow 3.5$ kA, as seen in Fig.1(a), resulting in fast and stable sys-
 235 tem optimization. This interesting example shows uncommon *positive effect*^{43,44} of self-organized
 236 transport on pedestal confinement.

237 We note that such an RMP-induced hysteresis shown in Fig5 is not trivial to be produced in
 238 the experiment as it conventionally requires a delicate pre-programmed RMP waveform. This
 239 leads to difficulties in investigating and exploiting the hysteresis, which is critical to optimize
 240 the ELM-free state. In this respect, adaptive RMP control is an effective methodology as it can
 241 automatically generate the hysteresis and utilize it. In addition, the adaptive scheme has been suc-
 242 cessfully operated for more than a hundred confinement times (~ 5 s) of KSTAR, and therefore,

243 this control is also expected to be applicable to long pulse plasma in ITER.

244

245 **The origin of broadened ion-pedestal.** It is worth pointing out that successful adaptive con-
246 trol in these experiments is mainly due to a broadened ion pedestal during the ELM suppression
247 phase. As shown in Fig.7a, the ion heat diffusivity (χ_i) of the pedestal region rapidly increases
248 via additional transport after transitions to the ELM-free state. In addition, the pedestal heat dif-
249 fusivity does not change much during 7.1-7.7 s, indicating that it is insensitive to the decreasing
250 I_{RMP} . It has been reported that the neoclassical transport effect dominates ion heat transport under
251 RMPs^{37,38}. However, this collisional transport strongly depends on the RMP strength. There-
252 fore, the broadened ion pedestal does not seem to be related to the neoclassical process. Here,
253 χ_i at $\psi_N = 0.96$ exceeds neoclassical level ($\geq 0.4\text{m}^2/\text{s}$) in all cases, supporting the existence of
254 additional transport.

255 Fluctuation measurements on KSTAR ($k_y\rho_s < 0.1$) reveal significant edge turbulence triggered
256 by RMPs^{25,26,45} after ELM suppression, where k_y is the bi-normal wave number, $\rho_s = \sqrt{2m_i T_e}/eB$
257 is the hybrid Larmor radius, and m_i is deuterium mass. Fig.7c, d illustrate the spectrogram and the
258 coherence strength of δT_e and δn_e fluctuations at $\psi_N \sim 0.96$. Fig.7e shows the poloidal magnetic
259 field fluctuations (δB_{pol}) at the inner wall. Here, δT_e and δn_e have strong coherence over the
260 frequency range of 20-100 kHz. The magnetic fluctuations in the 80-400 kHz range are also
261 observed during the same period. As shown in Fig.7f, they show an immediate instigation of
262 turbulence as ELM suppression begins followed by quick saturation within 200 ms. We note that
263 coherence before 6.4 s comes from ELM noise, and a magnetic signal of <50 kHz is responsible
264 for core modes. It is noteworthy that the strength of coherent fluctuations remains almost identical
265 during 7.1-7.7 s. Here, the widening of the ion pedestal coincides with the occurrence of edge
266 fluctuations. Furthermore, they are both insensitive to RMP strength. Therefore, these similarities
267 support the claim that the ion pedestal is widened primarily due to increased heat diffusivity by
268 edge turbulence.

269 Linear gyrokinetic simulations confirms that enhanced edge turbulence may occur in the ELM
270 suppression phase. As shown in Fig.7b, the linear growth rates (γ/γ_E) of turbulence mode exceed
271 the onset limit (>1) after the transitions to the ELM-free state. This is mainly due to decreased
272 stabilizing effect from the ExB shearing rate (γ_E)^{46,47}, which comes from the degraded pressure
273 pedestal (Fig.4b). It turns out that the excited modes are correlated with the ITG/TEM hybrid.
274 Here, the bi-normal wave length $k_y\rho_s \sim 0.3$ and real frequency ~ 51 kHz of the most unstable

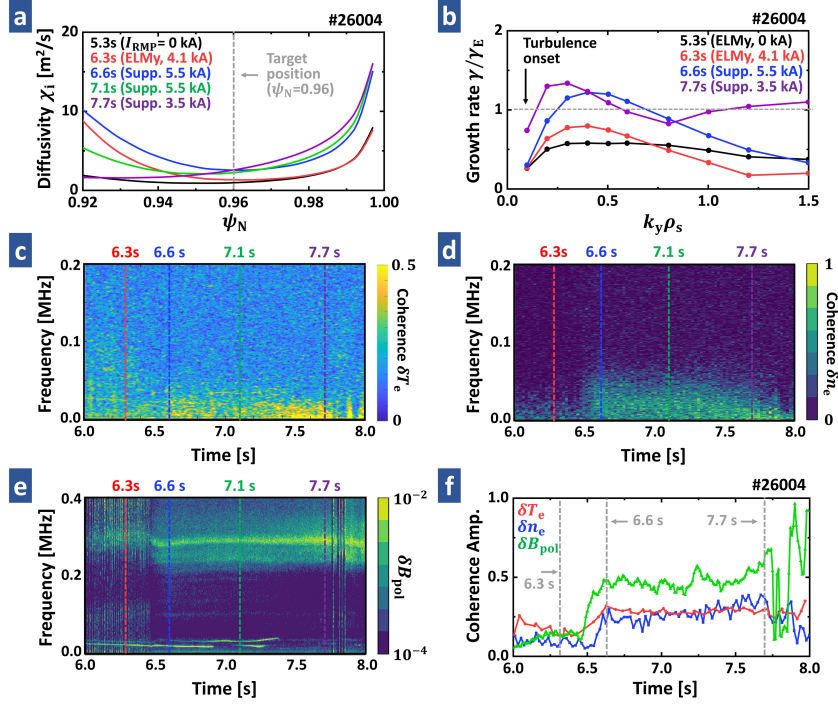


FIG. 7. **A broadened ion temperature pedestal by RMP-induced transport during ELM-suppression state.** **a** Radial profiles of ion heat diffusivity (χ_i) for five different time slices. **b** The growth rates of instability calculated from Gyro-kinetic simulation code CGYRO. **c** Coherence of edge T_e fluctuation from Electron cyclotron emission imaging system. **d** Coherence of edge n_e fluctuation from Beam emission imaging system. **e** Measured δB_{pol} fluctuation at inner wall from Mirnov coil. **f** Time trace of normalized integrated coherence amplitude of T_e (red), n_e (blue), and B_{pol} (green) fluctuations over the frequency space.

275 mode exhibits similar properties to the measured fluctuations of electron channels. The simulation
 276 results show that ion thermal diffusion can be increased with these unstable modes, supporting the
 277 idea of ion pedestal broadening by turbulence. However, theoretical analysis on RMP-induced tur-
 278 bulence still has many missing pieces. Recent studies have shown that the characteristics of trans-
 279 port in the presence of RMP deviates significantly from linear gyrokinetic calculations, raising
 280 the importance of non-linearity⁴⁸ and non-locality⁴⁹. In the future, nonlinear gyrokinetic studies
 281 including these effects will shed further light on the accurate description of edge turbulence under
 282 RMPs.

283 The considerable effect of RMP-induced transport on ion heat diffusion might inconsistent with
 284 the general trend of other devices^{16,17,32}, where such turbulence mainly affects electron channel
 285 and has a minor effect on ion transport. Although it is difficult to evaluate the turbulence effect

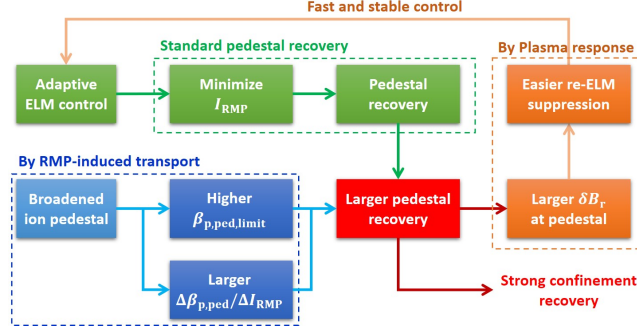


FIG. 8. **Schematic diagram of correlation between adaptive ELM control and pedestal recovery.** Here, it is noteworthy that the strong recovery of confinement is also attributable to the widened ion pedestal by RMP-induced transport during ELM suppression phase.

286 on n_e and T_e due to limitations in the diagnostics, we still confirm that there is a clear correlation
 287 between edge fluctuation and ion pedestal. Therefore, this observation suggests new possible role
 288 of turbulence on the ion pedestal under the low- $n(= 1)$ RMP and ELM-free states.

289 II. DISCUSSION

290 We have achieved successful optimization of a controlled ELM-free state with highly recov-
 291 ered confinement by $\sim 60\%$, maintaining $\beta_N \sim 1.91$, $\beta_p \sim 1.53$, and $H_{98} \sim 0.9$, with the original
 292 degradation in fusion gain largely recovered. This novel adaptive approach exhibits compatibility
 293 between RMP ELM suppression and high confinement. In addition, it provides a reliable strategy
 294 to achieve stable ELM-free access by preventing RMP-induced disruption. It is noteworthy that
 295 the remarkable recovery of confinement is not solely attributable to adaptive RMP control but also
 296 to a widened ion pedestal resulting from RMP-induced transport that promotes pedestal recovery
 297 by improving the ion response and ELM stability and facilitates fast, stable, and reinforced control
 298 optimization (Fig.8). This feature, which can be correlated to the turbulent process, is a good ex-
 299 ample of a system that transitions to an optimal state through a self-organized response to adaptive
 300 modulation. These results with low $n = 1$ RMP confirm that adaptive ELM control is a highly
 301 promising approach towards optimizing the ELM-free state, potentially solving one of the most
 302 challenging obstacles for viable and economical fusion energy.

303 However, there are remaining features to be improved for a “complete” adaptive ELM control
 304 picture. As shown in Fig.1a, the current approach is based on ELM detection and thereby in-

305 evitably faces several ELMs during control. This limitation could be critical at the reactor level,
306 where a single ELM can already be dangerous. Thus, a way to detect the loss of ELM suppression
307 in advance of the ELM re-occurrence is needed. Here, the behavior of edge turbulence suggests
308 the potential solution. The amplitude of magnetic fluctuation during the ELM-free phase shows a
309 rapid decrease 70 ms before the return of ELMs at 7.75 s (Fig.7f). Such an abrupt change in mag-
310 netic signals is an effective indicator of suppression loss. Therefore, this property can be utilized
311 in real-time to entirely avoid the return of ELM to achieve truly ELM-free optimization.

312 Previous work has shown that the effectiveness of RMP ELM suppression can be enhanced by
313 physics model-based 3D geometric optimization⁵⁰. Since this adaptive ELM control scheme max-
314 imizes the plasma performance for a given scenario, any additional improvements from external
315 forces will be augmented by the adaptive scheme. This makes the adaptive approach a prime can-
316 didate to fully exploit existing physics models for RMP ELM suppression. Future integration of
317 these features will lead to broader operational freedom and higher confinement recovery, as well
318 as the development of advanced ELM control techniques for ITER and future tokamaks.

319 III. METHODS

320 **KSTAR tokamak.** The KSTAR tokamak is the largest magnetic fusion devices in Republic of
321 Korea, supported by the Korea Institute of Fusion Energy (KFE) and the Government funds. It has
322 the plasma major radius $R_0 = 1.8$ m, minor radius $a_0 = 0.45$ m, and the toroidal magnetic field
323 $B_T = 1.8 - 2.3$ T at major radius R_0 . The $n = 1$ RMP ELM suppression discharge on KSTAR can
324 be reproduced at a lower electron density regime (.e.g., Greenwald density fraction ~ 0.4) with a
325 plasma shape having elongation $\kappa \sim 1.71$, upper triangularity $\delta_{up} \sim 0.37$, and upper triangularity
326 $\delta_{low} \sim 0.85$.

327
328 **Radial profile reconstruction.** Core ion temperature is measured by charge exchange recomb-
329 ination system⁵¹ for Carbon (6+) impurities at outboard mid-plane. Core electron temperature is
330 measured by the Thomson Scattering⁵² and Electron Cyclotron emission⁵³ system. Core electron
331 density is measured by the Thomson Scattering and Two-color interferometry system⁵⁴. To obtain
332 well-resolved profiles, the data are averaged over 100 ms. The pedestal height is obtained from
333 hyperbolic tangent fits with edge profiles. The equilibria from EFIT code⁵⁵ is used for the radial
334 profile mapping and fitting.

335

336 **Kinetic equilibria reconstruction.** Kinetic equilibria are reconstructed for the plasma stability
337 analysis. This equilibrium is calculated from the magnetic reconstruction using EFIT code with
338 the pressure profile (summation of thermal pressure profile from radial profile reconstruction and
339 fast ion pressure from NUBEAM code⁵⁶) and current density profile (core current from motional
340 Stark effect diagnostics⁵⁷ and edge current using NUBEAM, Ohmic and Sauter current models⁵⁸)
341 as a constraint. An iteration scheme is employed to update the thermal profiles, NUBEAM results,
342 and edge current calculation with new kinetic equilibrium.

343

344 **Pedestal stability calculation.** The pedestal stability (or ELM stability) limit is predicted using
345 the EPED1⁵⁹ algorithm. The fixed-boundary equilibrium code, CHEASE⁶⁰, is used for accurate
346 equilibrium mapping, and the ideal MHD stability code, MISHKA1⁶¹, is employed for ideal
347 peeling-ballooning³ stability calculation. The linear initial value solver is used to calculate the
348 most unstable mode. All other required parameters are taken from the reconstructed radial profiles
349 and plasma equilibrium.

350

351 **Ideal plasma response calculation.** The perturbed radial fields (δB_r) from an ideal plasma re-
352 sponse by RMP are calculated using IPEC code⁶² and given magnetic equilibria and I_{RMP} . The
353 core and edge responses are derived through radially averaging δB_r at $\psi_N = 0 - 0.9$ and $0.9 - 1.0$,
354 respectively. The thresholds of δB_r for RMP-induced ELM suppression and disruption are ob-
355 tained from neighboring experiments. The disruption thresholds in I_{RMP} are equivalent to the δB_r
356 thresholds based on the plasma response calculation.

357

358 **Plasma fluctuation measurements.** In this work, edge T_e and n_e fluctuations ($k_\perp \rho < 1$) are
359 measured from electron emission image spectroscopy (ECEI)⁶³ and beam emission spectroscopy
360 (BES)⁶⁴, respectively. Magnetic field perturbations are captured by the Mirnov coil signal (MC)⁶⁵.
361 The spectrogram of measured fluctuation is derived using Fourier transform. Coherence of elec-
362 tron density and temperature fluctuation is calculated from bi-spectrum analysis with two radially
363 adjacent channels in ECEI and BES, respectively. The ELM peaks and core modes are statistically
364 removed from integrating the amplitude of coherent fluctuations in all channels.

365

366 **Gyro-kinetic simulation.** The gyrokinetic code, CGYRO⁶⁶, is used in the linear analysis of

367 micro-instabilities. The linear initial value solver is employed to find the unstable mode in the
368 target radial point with wavelength $k_y \rho_s = 0.1 - 1.5$. This simulation is based on a flux-tube ap-
369 proach with a full gyro-kinetic description for both electron and ion channels. The reconstructed
370 radial profiles and kinetic equilibrium described above are included for the accurate modeling.
371 This calculation is performed at $\psi_N = 0.96$, where the changes of experimental fluctuations are
372 robust.

373

374 **IV. ACKNOWLEDGMENTS**

375 The authors would like to thanks KSTAR team. This material was supported by the U.S. Depart-
376 ment of Energy, under Awards DE-SC0020372. This research was also supported by R&D Pro-
377 gram of "KSTAR Experimental Collaboration and Fusion Plasma Research(EN2021-12)" through
378 the Korea Institute of Fusion Energy(KFE) funded by the Government funds.

379 **V. AUTHOR CONTRIBUTIONS**

380 S.K. and R.S. led the experimental demonstration and analysis. R.S. and S.K. develop the adaptive
381 controller. E.K. conceived the original idea of adaptive control. A.O.N. analyzed the micro insta-
382 bility with Gyro-kinetic code. S.H., S.Y., J.W. and Y.M. participated in all the experimental pro-
383 cedures and support the analysis. R.N. and Y.I. discussed the critical physics picture of ion-scale
384 turbulence and other transports at the pedestal. J.P. and Y.S. discussed the role of RMP response,
385 stability and transport analysis of pedestal region. C.Y conducted the interpretive transport analy-
386 sis using ASTRA. J.L. and J.K. analyzed the measured edge fluctuation in electron channel. S.K.
387 wrote the main manuscript text and A.O.N. and all authors reviewed it.

388 **VI. ADDITIONAL INFORMATION**

389 Competing financial interests: The authors declare no competing financial interests.

REFERENCES

¹F. Wagner, G. Fussmann, T. Grave, M. Keilhacker, M. Kornherr, K. Lackner, K. McCormick, E. R. Müller, A. Stäbler, G. Becker, K. Bernhardt, U. Ditte, A. Eberhagen, O. Gehre, J. Gernhardt, G. v. Gierke, E. Glock, O. Gruber, G. Haas, M. Hesse, G. Janeschitz, F. Karger, S. Kissel, O. Klüber, G. Lisitano, H. M. Mayer, D. Meisel, V. Mertens, H. Murmann, W. Poschenrieder, H. Rapp, H. Röhr, F. Ryter, F. Schneider, G. Siller, P. Smeulders, F. Söldner, E. Speth, K. H. Steuer, Z. Szymanski, and O. Vollmer, en“Development of an Edge Transport Barrier at the H-Mode Transition of ASDEX,” *Physical Review Letters* **53**, 1453–1456 (1984).

²A. Sips, J. Schweinzer, T. Luce, S. Wolfe, H. Urano, J. Hobirk, S. Ide, E. Joffrin, C. Kessel, S. Kim, P. Lomas, I. Nunes, T. Pütterich, F. Rimini, W. Solomon, J. Stober, F. Turco, P. de Vries, JET Contributors, The ASDEX Upgrade team, The DIII-D team, The C-Mod team, The JT-60U team, and ITPA-IOS TG members and experts, en“Assessment of the baseline scenario at $q_{95} \sim 3$ for ITER,” *Nuclear Fusion* **58**, 126010 (2018).

³J. W. Connor, R. J. Hastie, H. R. Wilson, and R. L. Miller, en“Magnetohydrodynamic stability of tokamak edge plasmas,” *Physics of Plasmas* **5**, 2687–2700 (1998).

⁴A. Loarte, G. Huijsmans, S. Futatani, L. Baylor, T. Evans, D. M. Orlov, O. Schmitz, M. Becoulet, P. Cahyna, Y. Gribov, A. Kavin, A. Sashala Naik, D. Campbell, T. Casper, E. Daly, H. Frerichs, A. Kischner, R. Laengner, S. Lisgo, R. Pitts, G. Saibene, and A. Wingen, en“Progress on the application of ELM control schemes to ITER scenarios from the non-active phase to DT operation,” *Nuclear Fusion* **54**, 033007 (2014).

⁵J. Gunn, S. Carpentier-Chouchana, F. Escourbiac, T. Hirai, S. Panayotis, R. Pitts, Y. Corre, R. Dejarnac, M. Firdaouss, M. Kočan, M. Komm, A. Kukushkin, P. Languille, M. Missirlian, W. Zhao, and G. Zhong, en“Surface heat loads on the ITER divertor vertical targets,” *Nuclear Fusion* **57**, 046025 (2017).

⁶T. E. Evans, R. A. Moyer, P. R. Thomas, J. G. Watkins, T. H. Osborne, J. A. Boedo, E. J. Doyle, M. E. Fenstermacher, K. H. Finken, R. J. Groebner, M. Groth, J. H. Harris, R. J. L. Haye, C. J. Lasnier, S. Masuzaki, N. Ohyabu, D. G. Pretty, T. L. Rhodes, H. Reimerdes, D. L. Rudakov, M. J. Schaffer, G. Wang, and L. Zeng, “Suppression of Large Edge-Localized Modes in High-Confinement DIII-D Plasmas with a Stochastic Magnetic Boundary,” *Physical Review Letters* **92** (2004), 10.1103/physrevlett.92.235003, publisher: American Physical Society (APS).

- 420 ⁷W. Suttrop, T. Eich, J. C. Fuchs, S. Günter, A. Janzer, A. Herrmann, A. Kallenbach, P. T. Lang,
421 T. Lunt, M. Maraschek, R. M. McDermott, A. Mlynek, T. Pütterich, M. Rott, T. Vierle, E. Wol-
422 frum, Q. Yu, I. Zammuto, and H. Zohm, en“First Observation of Edge Localized Modes Mit-
423 igation with Resonant and Nonresonant Magnetic Perturbations in ASDEX Upgrade,” *Physical*
424 *Review Letters* **106**, 225004 (2011).
- 425 ⁸Y. M. Jeon, J.-K. Park, S. W. Yoon, W. H. Ko, S. G. Lee, K. D. Lee, G. S. Yun, Y. U. Nam, W. C.
426 Kim, J.-G. Kwak, K. S. Lee, H. K. Kim, and H. L. Yang, “Suppression of Edge Localized Modes
427 in High-Confinement KSTAR Plasmas by Nonaxisymmetric Magnetic Perturbations,” *Physical*
428 *Review Letters* **109** (2012), 10.1103/physrevlett.109.035004, publisher: American Physical So-
429 ciety (APS).
- 430 ⁹Y. Sun, Y. Liang, Y. \. e. Liu, S. Gu, X. Yang, W. Guo, T. Shi, M. Jia, L. Wang, B. Lyu, C. Zhou,
431 A. Liu, Q. Zang, H. Liu, N. Chu, H. \. e. Wang, T. Zhang, J. Qian, L. Xu, K. He, D. Chen,
432 B. Shen, X. Gong, X. Ji, S. Wang, M. Qi, Y. Song, Q. Yuan, Z. Sheng, G. Gao, P. Fu, and
433 B. Wan, “Nonlinear Transition from Mitigation to Suppression of the Edge Localized Mode
434 with Resonant Magnetic Perturbations in the EAST Tokamak,” *Physical Review Letters* **117**
435 (2016), 10.1103/physrevlett.117.115001, publisher: American Physical Society (APS).
- 436 ¹⁰M. E. Fenstermacher, T. E. Evans, T. H. Osborne, M. J. Schaffer, M. P. Aldan, J. S. deGrassie,
437 P. Gohil, I. Joseph, R. A. Moyer, P. B. Snyder, R. J. Groebner, M. Jakubowski, A. W. Leonard,
438 O. Schmitz, and the DIII-D Team, en“Effect of island overlap on edge localized mode suppres-
439 sion by resonant magnetic perturbations in DIII-D,” *Physics of Plasmas* **15**, 056122 (2008).
- 440 ¹¹F. L. Waelbroeck, I. Joseph, E. Nardon, M. Bécoulet, and R. Fitzpatrick, “Role of singular layers
441 in the plasma response to resonant magnetic perturbations,” *Nuclear Fusion* **52**, 074004 (2012),
442 publisher: IOP Publishing.
- 443 ¹²Q. M. Hu, R. Nazikian, B. A. Grierson, N. C. Logan, J.-K. Park, C. Paz-Soldan, and Q. Yu, “The
444 density dependence of edge-localized-mode suppression and pump-out by resonant magnetic
445 perturbations in the DIII-D tokamak,” *Physics of Plasmas* **26**, 120702 (2019), publisher: AIP
446 Publishing.
- 447 ¹³R. Fitzpatrick, “Theory of edge localized mode suppression by static resonant magnetic pertur-
448 bations in the DIII-D tokamak,” *Physics of Plasmas* **27**, 042506 (2020), publisher: AIP Publish-
449 ing.
- 450 ¹⁴Y. Liu, C. Paz-Soldan, L. Li, and Y. Sun, en“Role of 3D neoclassical particle flux in density
451 pump-out during ELM control by RMP in DIII-D,” *Nuclear Fusion* **60**, 036018 (2020).

- 452 ¹⁵V. Rozhansky, P. Molchanov, E. Kaveeva, S. Voskoboynikov, A. Kirk, E. Nardon, D. Coster, and
453 M. Tendler, en“Modelling of the edge plasma of MAST in the presence of resonant magnetic
454 perturbations,” *Nuclear Fusion* **51**, 083009 (2011).
- 455 ¹⁶S. Mordijck, R. A. Moyer, and G. R. McKee, en“Changes in density fluctuations as a result
456 of resonant magnetic perturbations correlate with the density inverse scale length,” *Physics of
457 Plasmas* **19**, 024504 (2012).
- 458 ¹⁷G. McKee, Z. Yan, C. Holland, R. Buttery, T. Evans, R. Moyer, S. Mordijck, R. Nazikian,
459 T. Rhodes, O. Schmitz, and M. Wade, en“Increase of turbulence and transport with resonant
460 magnetic perturbations in ELM-suppressed plasmas on DIII-D,” *Nuclear Fusion* **53**, 113011
461 (2013).
- 462 ¹⁸H. Müller, T. Lunt, W. Suttrop, T. Eich, R. Fischer, J. Fuchs, A. Herrmann, M. Kočan,
463 P. de Marné, and E. Wolfrum, en“Modification of scrape-off layer transport and turbulence by
464 non-axisymmetric magnetic perturbations in ASDEX Upgrade,” *Journal of Nuclear Materials*
465 **438**, S64–S71 (2013).
- 466 ¹⁹N. Vianello, C. Rea, M. Agostini, R. Cavazzana, G. Ciaccio, G. De Masi, E. Martines, A. Mazzi,
467 B. Momo, G. Spizzo, P. Scarin, M. Spolaore, P. Zanca, M. Zuin, L. Carraro, P. Innocente,
468 L. Marrelli, M. E. Puiatti, and D. Terranova, en“Magnetic perturbations as a viable tool for
469 edge turbulence modification,” *Plasma Physics and Controlled Fusion* **57**, 014027 (2015).
- 470 ²⁰C. Rea, N. Vianello, M. Agostini, R. Cavazzana, G. De Masi, E. Martines, B. Momo, P. Scarin,
471 S. Spagnolo, G. Spizzo, M. Spolaore, and M. Zuin, en“Comparative studies of electrostatic tur-
472 bulence induced transport in presence of resonant magnetic perturbations in RFX-mod,” *Nuclear
473 Fusion* **55**, 113021 (2015).
- 474 ²¹L. Cui, R. Nazikian, B. Grierson, E. Belli, T. Evans, N. Logan, D. Orlov, S. Smith, G. Staebler,
475 and P. Snyder, en“The energy confinement response of DIII-D plasmas to resonant magnetic
476 perturbations,” *Nuclear Fusion* **57**, 116030 (2017).
- 477 ²²S. Liu, N. Yan, Y. Liang, H. Zhang, J. Xu, G. Xu, L. Wang, R. Chen, G. Hu, Y. Ye, Y. Sun, T. Shi,
478 H. Wang, M. Wu, X. Wu, S. Gu, M. Jia, N. Chu, Q. Ma, Y. Wang, T. Zhang, X. Han, L. Chen,
479 J. Liu, S. Xu, H. Wang, N. Zhao, W. Zhang, J. Qian, L. Zeng, L. Xu, S. Wang, H. Liu, Q. Zang,
480 Y. Yu, L. Liao, X. Gong, and EAST, en“Edge turbulence characteristics and transport during
481 the ELM mitigation with $n = 1$ resonant magnetic perturbation on EAST,” *Nuclear Fusion* **60**,
482 082001 (2020).

- 483 ²³M. W. Jakubowski, T. E. Evans, M. E. Fenstermacher, M. Groth, C. J. Lasnier, A. W. Leonard,
484 O. Schmitz, J. G. Watkins, T. Eich, W. Fundamenski, R. A. Moyer, R. C. Wolf, L. B. Bay-
485 lor, J. A. Boedo, K. H. Burrell, H. Frerichs, J. S. deGrassie, P. Gohil, I. Joseph, S. Mordijck,
486 M. Lehnen, C. C. Petty, R. I. Pinsker, D. Reiter, T. L. Rhodes, U. Samm, M. J. Schaffer, P. B.
487 Snyder, H. Stoschus, T. Osborne, B. Unterberg, E. Unterberg, and W. P. West, “Overview of the
488 results on divertor heat loads in RMP controlled H-mode plasmas on DIII-D,” *Nuclear Fusion*
489 **49**, 095013 (2009), publisher: IOP Publishing.
- 490 ²⁴P. Snyder, K. Burrell, H. Wilson, M. Chu, M. Fenstermacher, A. Leonard, R. Moyer, T. Osborne,
491 M. Umansky, W. West, and X. Xu, en“Stability and dynamics of the edge pedestal in the low
492 collisionality regime: physics mechanisms for steady-state ELM-free operation,” *Nuclear Fusion*
493 **47**, 961–968 (2007).
- 494 ²⁵R. Nazikian, C. Paz-Soldan, J. \. e. Callen, J. \. e. deGrassie, D. Eldon, T. \. e. Evans, N. \. e.
495 Ferraro, B. \. e. Grierson, R. \. e. Groebner, S. \. e. Haskey, C. \. e. Hegna, J. \. e. King, N. \. e.
496 Logan, G. \. e. McKee, R. \. e. Moyer, M. Okabayashi, D. \. e. Orlov, T. \. e. Osborne, J.-K.
497 Park, T. \. e. Rhodes, M. \. e. Shafer, P. \. e. Snyder, W. \. e. Solomon, E. \. e. Strait, and
498 M. \. e. Wade, “Pedestal Bifurcation and Resonant Field Penetration at the Threshold of Edge-
499 Localized Mode Suppression in the DIII-D Tokamak,” *Physical Review Letters* **114** (2015),
500 10.1103/physrevlett.114.105002, publisher: American Physical Society (APS).
- 501 ²⁶C. Paz-Soldan, R. Nazikian, S. \. e. Haskey, N. \. e. Logan, E. \. e. Strait, N. \. e. Ferraro, J. \. e.
502 Hanson, J. \. e. King, M. \. e. Lanctot, R. \. e. Moyer, M. Okabayashi, J.-K. Park, M. \. e.
503 Shafer, and B. \. e. Tobias, “Observation of a Multimode Plasma Response and its Relation-
504 ship to Density Pumpout and Edge-Localized Mode Suppression,” *Physical Review Letters* **114**
505 (2015), 10.1103/physrevlett.114.105001, publisher: American Physical Society (APS).
- 506 ²⁷G. Lee, J. Kim, S. Hwang, C. Chang, H. Chang, M. Cho, B. Choi, K. Kim, K. Cho, S. Cho,
507 K. Choh, C. Choi, J. Choi, J. Choi, I. Choi, C. Do, T. Ha, J. Han, J. Hong, K. Hong, N. Hur,
508 I. Hwang, K. Im, H. Jhang, Y. Jung, B. Kim, D. Kim, G. Kim, H. Kim, J. Kim, J. Kim, W. Kim,
509 Y. Kim, K. Kwon, M. Kyum, B. Lee, D. Lee, H. Lee, J. Lee, S. Lee, H. Na, Y. Oh, J. Park,
510 H. Ri, Y. Ryoo, K. Song, H. Yang, J. Yang, B. Yoo, S. Yoo, N. Yoon, S. Yoon, G. You, K. You,
511 W. Choe, D.-I. Choi, S. Jeong, D. Lee, Y. Bae, H. Kang, G. Kim, I. Ko, W. Namkung, J. Oh,
512 Y. Bae, Y. Cho, B. Hong, G. Hong, C. Hwang, S. In, M. Ju, H. Lee, B. Oh, B. Yoon, S. Baang,
513 H. Choi, J. Hwang, M. Kim, Y. Kim, S. Lee, J. Yee, C. Yoon, K.-H. Chung, S. Hong, Y. Hwang,
514 S. Kim, Y. Kim, K. Chung, J. Lim, D. Ha, S. Oh, K. Ryu, Q. Wang, T. Ko, J. Joo, S. Suh, C. Choi,

515 J. Lee, Y. Lee, H. Shin, I. Song, J. Baek, I. Han, Y. Koh, P. Park, C. Ryu, J. Cho, D. Hwang,
516 Y. Kim, J. Schmidt, H. Park, G. Neilson, W. Reiersen, R. Simmons, S. Bernabei, F. Dahlgren,
517 L. Grisham, S. Jardin, C. Kessel, J. Manickam, S. Medley, N. Pomphrey, J. Sinnis, T. Brown,
518 R. White, K. Young, J. Schultz, P. Wang, L. Sevier, M. Carter, P. Ryan, D. Swain, D. Hill,
519 W. Nevins, and B. Braams, en“The KSTAR project: An advanced steady state superconducting
520 tokamak experiment,” *Nuclear Fusion* **40**, 575–582 (2000).

521 ²⁸I. P. E. G. o. C. Transport, I. P. E. G. o. C. Database, and I. P. B. Editors, “Chapter 2: Plasma
522 confinement and transport,” *Nuclear Fusion* **39**, 2175–2249 (1999).

523 ²⁹H. Zohm, en“On the Minimum Size of DEMO,” *Fusion Science and Technology* **58**, 613–624
524 (2010).

525 ³⁰F. Laggner, D. Eldon, A. Nelson, C. Paz-Soldan, A. Bortolon, T. Evans, M. Fenstermacher,
526 B. Grierson, Q. Hu, D. Humphreys, A. Hyatt, R. Nazikian, O. Meneghini, P. Snyder, E. Unter-
527 berg, E. Kolemen, and t. DIII-D team, en“Real-time pedestal optimization and ELM control
528 with 3D fields and gas flows on DIII-D,” *Nuclear Fusion* **60**, 076004 (2020).

529 ³¹Y. In, J.-K. Park, Y. M. Jeon, J. Kim, G. Y. Park, J.-W. Ahn, A. Loarte, W. H. Ko, H. H. Lee, J. W.
530 Yoo, J. W. Juhn, S. W. Yoon, and H. P. and, “Enhanced understanding of non-axisymmetric in-
531 trinsic and controlled field impacts in tokamaks,” *Nuclear Fusion* **57**, 116054 (2017), publisher:
532 IOP Publishing.

533 ³²C. Sung, G. Wang, T. L. Rhodes, S. P. Smith, T. H. Osborne, M. Ono, G. R. McKee, Z. Yan, R. J.
534 Groebner, E. M. Davis, L. Zeng, W. A. Peebles, and T. E. Evans, en“Increased electron temper-
535 ature turbulence during suppression of edge localized mode by resonant magnetic perturbations
536 in the DIII-D tokamak,” *Physics of Plasmas* **24**, 112305 (2017).

537 ³³M. Kim, J. Lee, W. H. Ko, S.-H. Hahn, Y. In, Y. M. Jeon, W. Suttrop, S. K. Kim, G. Y. Park, J.-W.
538 Juhn, and J. H. Lee, en“Pedestal electron collisionality and toroidal rotation during ELM-crash
539 suppression phase under $n = 1$ RMP in KSTAR,” *Physics of Plasmas* **27**, 112501 (2020).

540 ³⁴D. Eldon, E. Kolemen, J. Barton, A. Briesemeister, D. Humphreys, A. Leonard, R. Maingi,
541 M. Makowski, A. McLean, A. Moser, and P. Stangeby, en“Controlling marginally detached
542 divertor plasmas,” *Nuclear Fusion* **57**, 066039 (2017).

543 ³⁵T. Osborne, G. Jackson, Z. Yan, R. Maingi, D. Mansfield, B. Grierson, C. Chrobak, A. McLean,
544 S. Allen, D. Battaglia, A. Briesemeister, M. Fenstermacher, G. McKee, P. Snyder, and The
545 DIII-D Team, “Enhanced H-mode pedestals with lithium injection in DIII-D,” *Nuclear Fusion*
546 **55**, 063018 (2015).

- 547 ³⁶Q. Hu, R. Nazikian, B. Grierson, N. Logan, D. Orlov, C. Paz-Soldan, and Q. Yu, en“Wide Op-
548 erational Windows of Edge-Localized Mode Suppression by Resonant Magnetic Perturbations
549 in the DIII-D Tokamak,” *Physical Review Letters* **125**, 045001 (2020).
- 550 ³⁷V. Rozhansky, E. Kaveeva, P. Molchanov, I. Veselova, S. Voskoboynikov, D. Coster, A. Kirk,
551 S. Lisgo, and E. Nardon, en“Modification of the edge transport barrier by resonant magnetic
552 perturbations,” *Nuclear Fusion* **50**, 034005 (2010).
- 553 ³⁸E. Viezzer, M. Cavedon, P. Cano-Megias, E. Fable, E. Wolfrum, D. J. Cruz-Zabala, P. David,
554 R. Dux, R. Fischer, G. F. Harrer, F. M. Laggner, R. M. McDermott, U. Plank, T. Pütterich,
555 M. Willensdorfer, and the ASDEX Upgrade Team, en“Dynamics of the pedestal transport during
556 edge localized mode cycles at ASDEX Upgrade,” *Plasma Physics and Controlled Fusion* **62**,
557 024009 (2020).
- 558 ³⁹W. A. Houlberg, K. C. Shaing, S. P. Hirshman, and M. C. Zarnstorff, en“Bootstrap current
559 and neoclassical transport in tokamaks of arbitrary collisionality and aspect ratio,” *Physics of*
560 *Plasmas* **4**, 3230–3242 (1997).
- 561 ⁴⁰S. Mordijck, R. Moyer, N. Ferraro, M. Wade, and T. Osborne, en“The radial electric field as
562 a measure for field penetration of resonant magnetic perturbations,” *Nuclear Fusion* **54**, 082003
563 (2014).
- 564 ⁴¹J. Lee, Y. M. Jeon, Y. In, G. Y. Park, G. S. Yun, W. Lee, M. Kim, J. H. Lee, W. H. Ko, and H. K. P.
565 and, “Direct evidence of $E \times B$ flow changes at the onset of resonant magnetic perturbation-
566 driven edge-localized mode crash suppression,” *Nuclear Fusion* **59**, 066033 (2019), publisher:
567 IOP Publishing.
- 568 ⁴²J.-K. Park, Y. Jeon, Y. In, J.-W. Ahn, R. Nazikian, G. Park, J. Kim, H. Lee, W. Ko, H.-S. Kim,
569 N. C. Logan, Z. Wang, E. A. Feibush, J. E. Menard, and M. C. Zarnstroff, “3D field phase-
570 space control in tokamak plasmas,” *Nature Physics* **14**, 1223–1228 (2018), publisher: Springer
571 Science and Business Media LLC.
- 572 ⁴³X. Chen, K. Burrell, T. Osborne, W. Solomon, K. Barada, A. Garofalo, R. Groebner, N. Luh-
573 mann, G. McKee, C. Muscatello, M. Ono, C. Petty, M. Porkolab, T. Rhodes, J. Rost, P. Snyder,
574 G. Staebler, B. Tobias, Z. Yan, and the DIII-D Team, en“Stationary QH-mode plasmas with
575 high and wide pedestal at low rotation on DIII-D,” *Nuclear Fusion* **57**, 022007 (2017).
- 576 ⁴⁴R. Nazikian, C. Petty, A. Bortolon, X. Chen, D. Eldon, T. Evans, B. Grierson, N. Ferraro,
577 S. Haskey, M. Knolker, C. Lasnier, N. Logan, R. Moyer, D. Orlov, T. Osborne, C. Paz-Soldan,
578 F. Turco, H. Wang, and D. Weisberg, en“Grassy-ELM regime with edge resonant magnetic

579 perturbations in fully noninductive plasmas in the DIII-D tokamak,” *Nuclear Fusion* **58**, 106010
580 (2018).

581 ⁴⁵J. Lee, G. S. Yun, M. J. Choi, J.-M. Kwon, Y.-M. Jeon, W. Lee, N. C. Luhmann, and
582 H. K. Park, “Nonlinear Interaction of Edge-Localized Modes and Turbulent Eddies in Toroidal
583 Plasma under $n=1$ Magnetic Perturbation,” *Physical Review Letters* **117** (2016), 10.1103/phys-
584 revlett.117.075001, publisher: American Physical Society (APS).

585 ⁴⁶H. Biglari, P. H. Diamond, and P. W. Terry, “Influence of sheared poloidal rotation on edge
586 turbulence,” *Physics of Fluids B: Plasma Physics* **2**, 1–4 (1990), publisher: AIP Publishing.

587 ⁴⁷T. S. Hahm and K. H. Burrell, “Flow shear induced fluctuation suppression in finite aspect ratio
588 shaped tokamak plasma,” *Physics of Plasmas* **2**, 1648–1651 (1995), publisher: AIP Publishing.

589 ⁴⁸R. Hager, C. S. Chang, N. M. Ferraro, and R. Nazikian, en“Gyrokinetic understanding of the
590 edge pedestal transport driven by resonant magnetic perturbations in a realistic divertor geome-
591 try,” *Physics of Plasmas* **27**, 062301 (2020), arXiv: 2003.07130.

592 ⁴⁹S. Taimourzadeh, L. Shi, Z. Lin, R. Nazikian, I. Holod, and D. Spong, en“Effects of RMP-
593 induced changes of radial electric fields on microturbulence in DIII-D pedestal top,” *Nuclear*
594 *Fusion* **59**, 046005 (2019).

595 ⁵⁰S. Yang, J.-K. Park, N. Logan, C. Zhu, Q. Hu, Y. Jeon, Y. In, W. Ko, S. Kim, Y. Lee, and
596 Y. Na, “Localizing resonant magnetic perturbations for edge localized mode control in KSTAR,”
597 *Nuclear Fusion* **60**, 096023 (2020).

598 ⁵¹Won-Ha Ko, Seungtae Oh, and Myeun Kwon, en“KSTAR Charge Exchange Spectroscopy Sys-
599 tem,” *IEEE Transactions on Plasma Science* **38**, 996–1000 (2010).

600 ⁵²J. H. Lee, S. Oh, H. M. Wi, W. R. Lee, K. P. Kim, K. team, I. Yamada, K. Narihara, and
601 K. Kawahata, en“Tangential Thomson scattering diagnostic for the KSTAR tokamak,” *Journal*
602 *of Instrumentation* **7**, C02026–C02026 (2012).

603 ⁵³G. S. Yun, W. Lee, M. J. Choi, J. B. Kim, H. K. Park, C. W. Domier, B. Tobias, T. Liang,
604 X. Kong, N. C. Luhmann, and A. J. H. Donné, en“Development of KSTAR ECE imaging
605 system for measurement of temperature fluctuations and edge density fluctuations,” *Review of*
606 *Scientific Instruments* **81**, 10D930 (2010).

607 ⁵⁴K. Lee, J.-W. Juhn, Y. Nam, Y. Kim, H. Wi, S. Kim, and Y.-c. Ghim, en“The design of two color
608 interferometer system for the 3-dimensional analysis of plasma density evolution on KSTAR,”
609 *Fusion Engineering and Design* **113**, 87–91 (2016).

610 ⁵⁵L. Lao, H. St. John, R. Stambaugh, A. Kellman, and W. Pfeiffer, en“Reconstruction of current
611 profile parameters and plasma shapes in tokamaks,” *Nuclear Fusion* **25**, 1611–1622 (1985).

612 ⁵⁶A. Pankin, D. McCune, R. Andre, G. Bateman, and A. Kritz, en“*The tokamak Monte Carlo fast
613 ion module NUBEAM in the National Transport Code Collaboration library,*” *Computer Physics
614 Communications* **159**, 157–184 (2004).

615 ⁵⁷J. Chung, J. Ko, J. Howard, C. Michael, G. v. Nessi, A. Thorman, and M. F. M. D. Bock,
616 “Motional Stark effect diagnostics for KSTAR,” *Journal of the Korean Physical Society* **65**,
617 1257–1260 (2014), publisher: Korean Physical Society.

618 ⁵⁸O. Sauter, C. Angioni, and Y. R. Lin-Liu, en“Neoclassical conductivity and bootstrap current
619 formulas for general axisymmetric equilibria and arbitrary collisionality regime,” *Physics of
620 Plasmas* **6**, 2834–2839 (1999).

621 ⁵⁹P. B. Snyder, R. J. Groebner, A. W. Leonard, T. H. Osborne, and H. R. Wilson, en“Development
622 and validation of a predictive model for the pedestal height,” *Physics of Plasmas* **16**, 056118
623 (2009).

624 ⁶⁰H. Lütjens, A. Bondeson, and O. Sauter, “The CHEASE code for toroidal MHD equilibria,”
625 *Computer Physics Communications* **97**, 219–260 (1996), publisher: Elsevier BV.

626 ⁶¹A. Mikhailovskii, G. Huysmans, W. Kerner, and S. Sharapov, “Optimization of computational
627 MHD normal-mode analysis for tokamaks,” *Plasma Physics Reports* **23**, 844–857 (1997).

628 ⁶²J.-k. Park, A. H. Boozer, and A. H. Glasser, en“Computation of three-dimensional tokamak and
629 spherical torus equilibria,” *Physics of Plasmas* **14**, 052110 (2007).

630 ⁶³G. S. Yun, W. Lee, M. J. Choi, J. Lee, M. Kim, J. Leem, Y. Nam, G. H. Choe, H. K. Park,
631 H. Park, D. S. Woo, K. W. Kim, C. W. Domier, N. C. Luhmann, N. Ito, A. Mase, and S. G. Lee,
632 “Quasi 3D ECE imaging system for study of MHD instabilities in KSTAR,” *Review of Scientific
633 Instruments* **85**, 11D820 (2014), publisher: AIP Publishing.

634 ⁶⁴Y. U. Nam, S. Zoletnik, M. Lampert, Kovácsik, and H. M. Wi, en“Edge electron density profiles
635 and fluctuations measured by two-dimensional beam emission spectroscopy in the KSTAR,”
636 *Review of Scientific Instruments* **85**, 11E434 (2014).

637 ⁶⁵J. G. Bak, S. G. Lee, D. Son, and the KSTAR Project Team, en“Performance of the magnetic
638 sensor and the integrator for the KSTAR magnetic diagnostics,” *Review of Scientific Instruments*
639 **75**, 4305–4307 (2004).

640 ⁶⁶J. Candy, E. Belli, and R. Bravenec, en“*A high-accuracy Eulerian gyrokinetic solver for colli-
641 sional plasmas,*” *Journal of Computational Physics* **324**, 73–93 (2016).